AIAA JOURNAL
Vol. 39, No. 5, May 2001

Improved Solid-Wall Boundary Treatment in Low-Reynolds-Number Turbulence Models

Patrik Rautaheimo* and Timo Siikonen†
Helsinki University of Technology, FIN-02015 HUT, Finland

For a low-Reynolds-number turbulence model, the boundary layer is solved accurately next to the solid boundaries. Generally, it is required that there is a sufficient number of computational points in a viscous sublayer. In this work the effect of the height of the first cell next to the solid surfaces is studied. Modifications to the momentum equation, to the energy equation, and also to the k–ϵ model that reduces the number of grid points needed in the viscous sublayer for an accurate result are suggested. It is shown that the accuracy of the simulation is enhanced when the proposed modifications are applied. For a coarse grid the stability is increased as well.

Nomenclature

B	=	constant in the universal wall function, 5.5
b	=	wing half-span
C_D	=	drag coefficient, $D/(\frac{1}{2}\rho u_{\text{ref}}^2 S)$
C_L	=	lift coefficient, $L/(\frac{1}{2}\rho u_{\text{ref}}^2 S)$
c_f	=	skin-friction coefficient, $\tau_w/(\frac{1}{2}\rho u_{\text{ref}}^2)$
c_μ	=	wall damping function for a low-Reynolds-number model
D	=	wall dissipation function, $2\nu(k/y^2)$
d_w	=	first cell height
F, G, H	=	flux vectors in the x, y, and z directions
H	=	channel height
i, j, k	=	grid coordinate directions
k	=	kinetic energy of turbulence
Ma	=	Mach number
P	=	production of the kinetic energy of turbulence
Pr	=	Prandtl number
Re	=	Reynolds number
S	=	cell-face area; reference area
Tu	=	turbulence intensity, $\sqrt{(\frac{2}{3}k/u_{\text{ref}}^2)}$
t	=	time
t_{turb}	=	turbulent time scale
U	=	vector of conservative variables
u, v, w	=	velocity components in the x, y, and z directions
u_τ	=	friction velocity, $\sqrt{(\tau_w/\rho)}$
x, y, z	=	Cartesian coordinates
y^+	=	nondimensional normal distance from the surface
α	=	weighting factor; angle of attack
ϵ	=	dissipation of the kinetic energy of turbulence
κ	=	von Kármán constant, $\approx$0.4
μ	=	dynamic viscosity
ν	=	kinematic viscosity
ρ	=	density
τ_w	=	surface shear stress

Subscripts

i	=	i index; summation index
ref	=	reference value
T	=	turbulent conditions
v	=	viscous value
x, y, z	=	component in the x, y, and z coordinate directions

Presented as Paper 2000-0136 at the AIAA 38th Aerospace Sciences Meeting, Reno, NV, 10–13 January 2000; received 28 February 2000; revision received 7 March 2000; accepted for publication 7 June 2000.

*Research Scientist, Laboratory of Applied Thermodynamics, P.O. Box 4400; Patrik.Rautaheimo@hut.fi. Member AIAA.

†Professor, Laboratory of Applied Thermodynamics, P.O. Box 4400; Timo.Siikonen@hut.fi. Member AIAA.

I. Introduction

WALL functions have long been used as an alternative in the calculation of wall-bounded turbulent flows. This means that the boundary conditions are applied in the first computational cell next to the solid surfaces instead of the solid boundary. Accordingly, the boundary cells should be located in the region where the wall function is valid. The benefit of using this boundary treatment is the relatively coarse grid density inside the boundary layer. Strictly speaking, the wall functions describe the flow accurately only for a flat-plate boundary layer with a zero or moderate pressure gradients.[1] For complex flow situations where flow is generally rapidly changing, the calculation should be extended onto the solid boundaries. This requires low-Reynolds-number modeling of turbulence.

Low-Reynolds-number k–ϵ models are among the most popular ways to simulate turbulent flows. The low-Reynolds-number models are very sensitive to the height of the first cell next to the solid boundary. Generally, the nondimensional height (y^+) of the first cell should not exceed a value of one. Consequently, computational meshes must be very dense with a high global Reynolds number. Recently, there have been some studies on how to lessen this restriction[2] by using a new universal wall-function type of approach.

In this study the effect of the first cell height is studied with Chien's k–ϵ model.[3] For the original model it is shown that the nondimensional first cell height should have a value less than two, if 1% accuracy is desired in the friction coefficient. Discretization methods for the flow equations that are not as sensitive to the first cell height will be designed. Furthermore, new methods of calculating boundary conditions are proposed, and results of test calculations are shown. The proposed methods will be applied for a channel flow, a zero pressure gradient boundary layer, the ONERA M6 wing, and the BAe Hawk trainer. Although these new methods are applied with one particular turbulence model, Chien's k–ϵ, most important refinements are directly applicable for any eddy-viscosity type approach.

II. Turbulent Boundary Layer

The turbulent boundary layer can be divided into four different layers[4]: viscous sublayer, buffer layer, overlap layer, and outer layer. Very near the wall, turbulence is damped out, and the boundary layer is dominated by the viscous shear. In this viscous sublayer the velocity profile is linear:

$$u^+ = y^+ \tag{1}$$

where $u^+ = u/u_\tau$ is a nondimensional velocity and $y^+ = yu_\tau/\nu$ is a nondimensional distance from the solid-wall boundary. Generally, y^+ has a value of five at the edge of the viscous layer. The velocity profile is very steep next to the solid wall. To get a feeling for how thin the viscous sublayer really is, consider the flow over a flat plate at a distance of 1 m from the leading edge with a speed of 10 m/s. In that case the friction velocity is $u_\tau \approx 0.44$ m/s

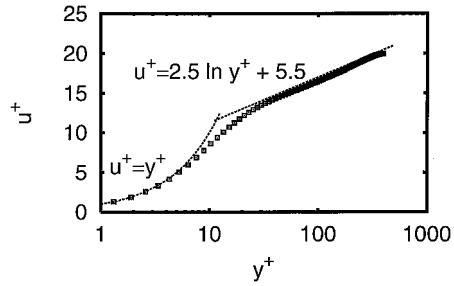

Fig. 1 Velocity profile in a turbulent boundary layer at $Re = 1.376 \times 10^4$.

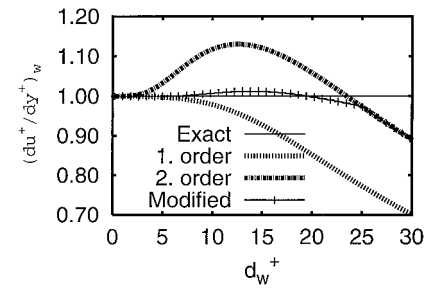

Fig. 2 Calculated velocity gradient at the wall as a function of the first cell height.

and $y(y^+ = 5) = 0.17$ mm. For a low-Reynolds-number model there should be a few computational points inside this viscous sublayer.

For the overlap layer the universal wall function is valid:

$$u^+ = (1/\kappa)\,\ell_n y^+ + B \tag{2}$$

where κ and B are constants and get values of 0.4 and 5.5, respectively. In a case of a channel flow, the velocity profile is given in Fig. 1. The Reynolds number, based on the channel height H and the bulk velocity u_{bulk},

$$Re = u_{\text{bulk}} H/\nu \tag{3}$$

is 13,760. The data are based on direct numerical simulation.[5]

III. Methods

In this chapter modifications to the momentum and turbulence equations are introduced. The following modifications do not change the results when the finest mesh spacing is approached but enhance the accuracy and robustness with coarse grids. The methods developed will be applied for a fully developed channel flow. The solution is obtained by using a semi-one-dimensional incompressible flow solver.[6] The test will be run with different first cell heights using a set of different methods. The grid is clustered so that the ratio of the neighboring cell heights is no more than 1.13. The Reynolds number of this flow is 10^5. For the skin-friction coefficient at this Reynolds number, White's[4] experimental function gives $c_f = 0.00428$, and the simulation with the finest mesh applied ($d_w^+ = 0.18$) results in $c_f = 0.00403$.

A. Momentum Equation

If the convective terms are neglected, the u-momentum equation with the eddy-viscosity assumption reduces close to the wall region to

$$\frac{\partial \rho u}{\partial t} + \frac{\partial p}{\partial x} = \frac{\partial}{\partial y}\left[(\mu + \mu_T)\frac{\partial u}{\partial y}\right] \tag{4}$$

The equation is written so that u velocity is parallel to the wall and the y coordinate is perpendicular to the wall. Using a cell-centered finite volume method, the preceding equation is solved as

$$U_i^{n+1} = U^n - (\Delta t/V_i)\left[F_{i+\frac{1}{2}} - F_{i-\frac{1}{2}} + G_{j+\frac{1}{2}} - G_{j-\frac{1}{2}}\right] \tag{5}$$

where V_i is the volume of a cell and Δt is a time step. The flux in the j direction is

$$G_{j+\frac{1}{2}} = -S_{j+\frac{1}{2}}\left[(\mu + \mu_T)\frac{\partial u}{\partial y}\right]_{j+\frac{1}{2}} \tag{6}$$

where $S_{j+1/2}$ is a cell face.

1. Wall Friction

Skin friction in the low-Reynolds-number turbulence models is directly calculated from the velocity gradient at the wall:

$$\tau_w = \mu\left(\frac{\partial u}{\partial y}\right)_{\text{wall}} \tag{7}$$

This derivative can be evaluated using a first- or second-order difference formula. These can be written as

$$\left(\frac{\partial u}{\partial y}\right)_{\text{wall,1.order}} = \frac{-u_w + u_1}{d_w/2} + \mathcal{O}(d_w) \tag{8}$$

$$\left(\frac{\partial u}{\partial y}\right)_{\text{wall,2.order}} = \frac{-8u_w + 9u_1 - u_2}{3d_w} + \mathcal{O}\left(d_w^2\right) \tag{9}$$

If a no-slip boundary condition is imposed, $u_w = 0$.

Next, the velocity profile of the turbulent boundary layer is used to study the accuracy of the finite difference equations (8) and (9). White[4] has deduced a single composite formula for a velocity profile that covers the wall-related regions (the viscous sublayer, the buffer layer, and the overlap layer):

$$y^+ = u^+ + e^{-\kappa B}\left[e^{\kappa u^+} - 1 - \kappa u^+ - (\kappa u^+)^2/2 - (\kappa u^+)^3/6\right] \tag{10}$$

where κ and B are defined in the preceding section. The nondimensional velocity u^+ is solved iteratively from the preceding equation, and an accuracy test of the derivatives is made. The exact derivative on the wall is easily found for the nondimensional variables by using Eq. (1). Figure 2 shows unexpected results. For a small first cell height the first-order approximation gives a more accurate derivative on the wall than the second-order approximation. If the height of the first cell is $d_w > 17$, the second-order difference formula gives better results. One must keep in mind that this is the situation for an equilibrium boundary layer. For nonequilibrium flows the situation could be different.

Because the error of the second-order method is larger close to the wall and smaller far away from the wall, a function that changes accuracy from the first- to the second-order method is designed:

$$\left(\frac{\partial u}{\partial y}\right)_{\text{wall}} = (1-\alpha)\left(\frac{\partial u}{\partial y}\right)_{\text{1.order}} + \alpha\left(\frac{\partial u}{\partial y}\right)_{\text{2.order}} \tag{11}$$

Here α is calculated from

$$\alpha = \min\left[\frac{Re_{(uy)_1}}{120}, 1\right], \qquad Re_{(uy)_1} = \frac{|u_1|y_1}{\nu} \tag{12}$$

where $Re_{(uy)_1}$ is a centerpoint Reynolds number of the first cell and y_1 is the corresponding distance from the solid boundary. This number reduces to $Re = u^+ y^+$ with nondimensional variables. If the new way of calculating the derivative is applied to Eq. (10), the accuracy is clearly improved, as seen in Fig. 2.

Next, a comparison is made using a one-dimensional channel flow simulation at $Re = 10^5$. The accuracy of the predicted skin-friction coefficient is evaluated as a function of the dimensionless height of the first cell d_w^+. The results are shown in Fig. 3, where the baseline model uses the second-order formula of Eq. (9); "Mod. 1" is based on Eq. (11), and "final" is the complete model proposed in this paper. It is seen that the maximum error compared to the baseline model is reduced from 18 to 11%. In the final model the effect of the derivate approximation is smaller. The modification of Eq. (11) improves the result by about 3%.

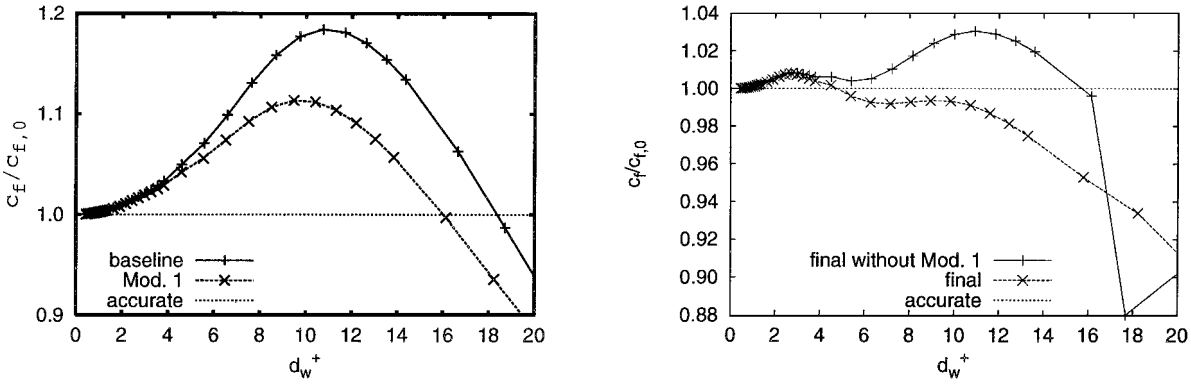

Fig. 3 Effect of the Reynolds-number-based derivative approximation (Mod. 1) on the solid wall for the channel flow calculation (on the left) and the effect of the derivative approximation (Mod. 1) in the final scheme (on the right).

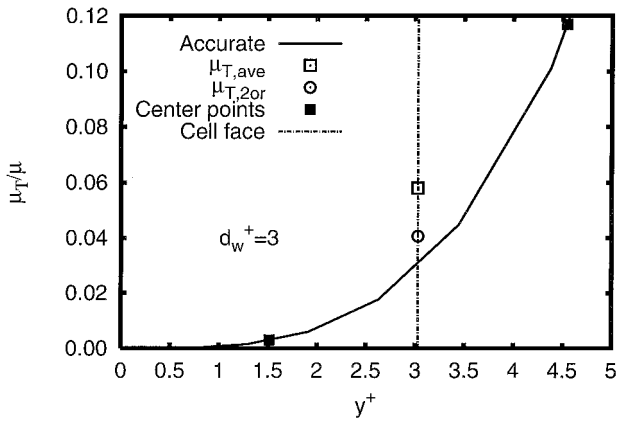

Fig. 4 Eddy viscosity in a channel flow with two different grid spacings. The eddy viscosity at the cell face is calculated by using averaging (ave) and Eq. (15) (2or); —— represents the accurate value.

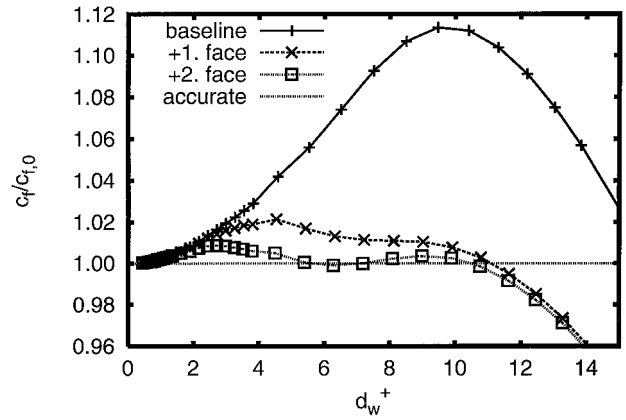

Fig. 5 Effect of the modified diffusion close to the wall on the channel flow calculation. The baseline model includes modifications made so far; in "+1. face" the diffusion is modified at the first computational face, and in "+2. face" the modification also includes the second face.

Equation (11) is also studied with fully developed laminar channel flow profile ($Re = u_{\text{bulk}}\delta/\nu = 2000$). Velocity profile is solved analytically, and it gave maximum error of 4% as $d_w^+ = 13$. In that case the second-order method would have been exactly correct because the laminar channel flow velocity profile is parabolic.

2. Turbulent Diffusion near the Solid Boundaries

In the following the calculation of the turbulent viscosity μ_T on the cell faces is studied. Generally, as the finite volume method is used, the eddy viscosity is evaluated as an average of the two adjacent cell values $\mu_{T,j+1/2} = \frac{1}{2}(\mu_{T,j} + \mu_{T,j+1})$. However, this can give inaccurate results if the first cell height d_w^+ is too large. The eddy viscosity has an asymptotic behavior near the wall as

$$\mu_T = \mathcal{O}(y^3) \tag{13}$$

Because the third-order equation would need four points to be solved and only three of them are practically available (wall point and cell points on both sides of the cell's common face), the eddy viscosity is assumed to have a second-order form in the vicinity of the wall:

$$\mu_T = Ay^2 + By + C \tag{14}$$

Using the values on the wall ($\mu_{T,w} = 0$) and at the cells $j = 1$ and 2 or 2 and 3, the following three point formulas are obtained:

$$\mu_{T,\frac{3}{2}} = \mu_{T,1} + \tfrac{1}{3}\mu_{T,2}, \qquad \mu_{T,\frac{5}{2}} = \tfrac{2}{3}\mu_{T,2} + \tfrac{2}{5}\mu_{T,3} \tag{15}$$

Instead of the averages these will be applied on the first two cell faces next to the solid wall. The resulting turbulent viscosities for a fine ($d_w^+ = 0.5$) and coarse grid ($d_w^+ = 3$) are shown in Fig. 4. The averaged viscosity value and Eq. (15) are used for the first cell face of the coarse grid at $d_w^+ = 3$. At the first computational cell face Eq. (15) gives a more accurate value for the turbulent viscosity than the average of the adjacent nodal viscosities. This justifies the use of a quadratic approximation for Eq. (14).

A test calculation is made to compare the baseline model that now contains the improvement of Eq. (11) to the modification of Eq. (15). The results are shown in Fig. 5. The relationships of Eq. (15) have a significant effect especially in the region of $3 < d_w^+ < 14$. Figure 5 also shows that it is not enough to modify the first cell face in the computational domain, but also the second cell face (at $j = \frac{5}{2}$) should be modeled according to Eq. (15). The biggest error is reduced from 12% to under 1%, as $d_w^+ < 11$. The error in Fig. 5 is different from that shown in Fig. 2, because in Fig. 5 the channel flow is solved and it includes more sources of errors than the direct application of Spalding's law.

B. Production

Production next to the solid boundary can be written with the eddy-viscosity model approximately as

$$P = \mu_T \left(\frac{\partial u}{\partial y}\right)^2 \tag{16}$$

The velocity derivative cannot be straightforwardly evaluated in the first cell next to the surface. Generally, the derivatives are calculated using central differences in the cell-centered scheme. However, if the consistency between the turbulence and momentum is taken into account, the solution is clear: The velocity gradients in the production term and in the momentum equation must be the same. The shear stress at the center of the first computational node is written as

$$\tau_w \approx \tau_1 = \left[(\mu + \mu_T)\frac{\partial u}{\partial y}\right]_1 \tag{17}$$

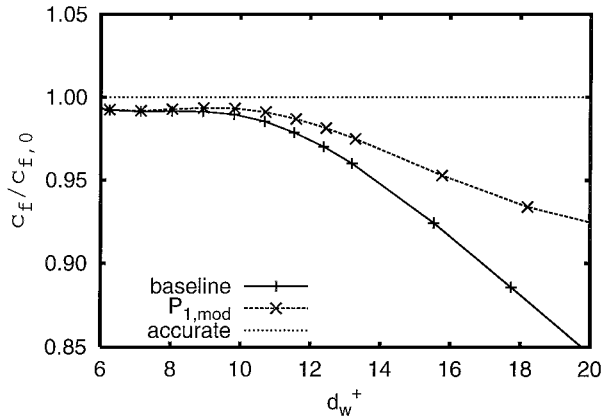

Fig. 6 Effect of the modification of the production term next to the wall.

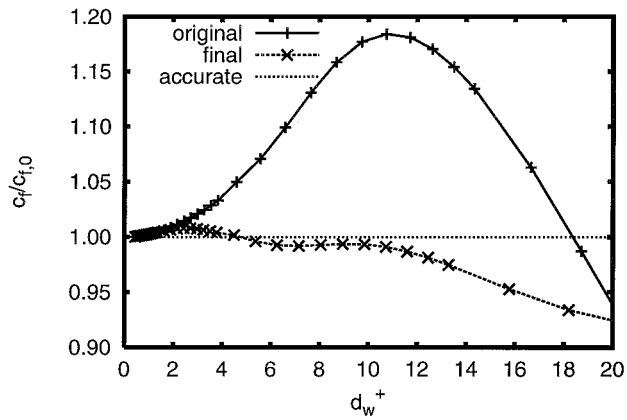

Fig. 7 Comparison between the final and the original models.

where the fact that shear stress is constant through the viscous sublayer is used. By obtaining the u derivative from this equation, the production of the turbulence Eq. (16) next to the surface takes the form

$$P_{1,\mathrm{mod}} = \mu_{T,1}\left[\tau_w^2 \big/ (\mu_1 + \mu_{T,1})^2\right] \tag{18}$$

The effect of this change on the channel flow case is shown in Fig. 6. This modification has an effect in the region of $8 < d_w^+ < 20$, where the results are significantly improved.

C. Model Summary

Now the modeling can be summarized as follows:

1) On the wall the velocity derivatives are calculated from Eq. (11).

2) Instead of the averages the turbulent viscosities are evaluated from Eq. (15).

3) The production of turbulent kinetic energy in the first cell is obtained from Eq. (18).

4) In the first cell the turbulence time scale is limited as[7]

$$t_{\mathrm{turb}} = \max\left(k/\epsilon,\ \sqrt{\nu/\epsilon}\right) \tag{19}$$

This limitation is applied only in the source term of the dissipation equation.

Furthermore, the temperature derivatives on the wall are calculated in the same way as the velocity derivatives, and the turbulent thermal conductivities are evaluated as the turbulent viscosities at the first and second cell faces next to the solid surface. Although the derivatives of k and $\tilde{\epsilon}$ are actually equal to zero on the solid wall, their calculation is modified.[8] This has only a minor effect on the results, but stability is improved.

A comparison between the original model and the model including all of the proposed modifications can be seen in Fig. 7. As far as the skin friction is concerned, the present model gives an accuracy of better than 1% up to $d_w^+ \approx 11$, where the original model has a 18% deviation in the skin-friction distribution. It is natural that a low-Reynolds-number model yields to unphysical results as d_w^+ is getting larger.

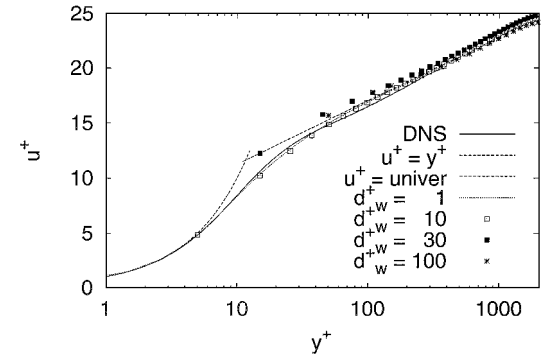

Fig. 8 Velocity profile with different grid sizes.

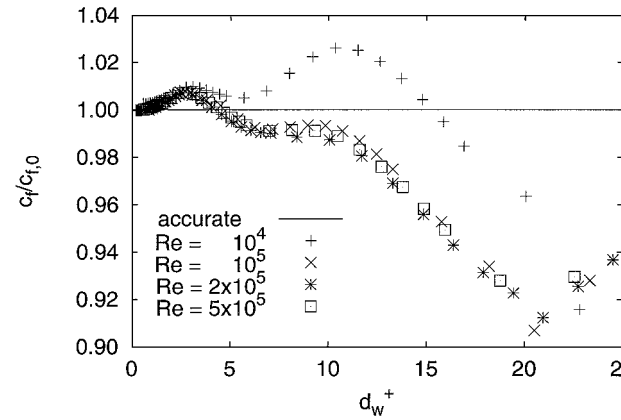

Fig. 9 Effect of the Reynolds number on the calculated skin-friction coefficient.

The velocity profiles with different d_w^+ values are shown in Fig. 8. In all cases the velocity profile is predicted with good accuracy. The effect of the global Reynolds number is also studied. The Reynolds number is varied from $Re = 10^4$ to 5×10^5. The normalized friction coefficients are plotted in Fig. 9. It is seen that the larger the Reynolds number, the better is the accuracy obtained with coarse grids when the present model is applied.

IV. Test Calculations

The solid-wall boundary treatment described in the preceding sections is implemented into a finite volume Navier–Stokes solver.[9] The flow solver uses a structured multiblock grid. In each block an implicit LU-factored solution with a spatial varying time step is performed. In this study the solution method is based on Roe's scheme.[10] The flux calculation uses MUSCL-type differencing with second-order upwinding in the streamwise direction and third-order upwind-biased discretization in the other directions. Turbulence is modeled by Chien's two-equation model. For the turbulence quantities the flux calculation uses second-order upwinding with a limiter of van Albada.[11] To accelerate the convergence, multigrid cycling[12] is used. When the multigrid is activated, turbulent viscosity is not evaluated on the coarse levels. Instead, the turbulent viscosities are transformed onto the coarse grid levels as the main flow variables. The boundary conditions between the blocks are treated explicitly and only on the highest grid level.

A. Flat-Plate Boundary Layer

The first test case is the flow over a flat plate with a high freestream turbulent intensity. The test case is taken from ERCOFTAC Fluid

Dynamics Database WWW Services kept by P. Voke (http://fluindigo.mech.surrey.ac.uk/). Experimental results for this flow case have been provided by John Coupland (Rolls–Royce).

The inlet velocity is 9.4 m/s, and the pressure gradient is zero. Measurements are made up to $x = 1.495$ m from the leading edge, which corresponds to $Re_x \approx 9.4 \times 10^5$. The upstream turbulence intensity (at the beginning of the flat plate) is $Tu = \sqrt{(\frac{2}{3}k)}/U = 6.0\%$. Dissipation is set so that the decay of a freestream turbulence is in balance.

The length of the flat plate is 1.6 m, but the calculation is started 16 cm before the plate. The height of the grid is 30 cm, and the height of the first cell next to the solid surface varies from 3.3 to 550 μm between the grids. This corresponds to $0.1 < d_w^+ < 13.1$. Grids are clustered to the wall except that the first two rows are of an equal size. The ratio of the heights between neighboring cells is $\Delta y_{j+1}/\Delta y_j = 1.1$. In the downstream or i direction 96 grid points are used for every grid density. In the j direction the number of grid points varies from 44 to 96.

At the inlet a uniform velocity distribution is assumed, and pressure is extrapolated from the computational domain. A symmetry condition is applied before the flat plate. At the flat plate the velocities and turbulence quantities are treated as described in this paper and compared to the original method. At the outlet zero gradients are assumed for the flow variables, but the pressure is given. The upper boundary, parallel to the wall, is assumed to have a zero gradient, except the u-velocity component and the pressure are set to constant values.

Convergence with different grid sizes is shown in Fig. 10. In these cases the Courant–Friedrichs–Lewy number is kept at a constant value of 10, and three multigrid sweeps are used. The present method is more stable and has a marginally better convergence rate with the coarse grids.

The normalized friction coefficient can be used to compare the accuracy of different grid sizes. Figure 11 shows the normalized friction coefficient as a function of the local Reynolds number. It is seen that the friction coefficient is better predicted with the present methods. With the coarsest grid the present method underestimates the skin friction by 5%, whereas the original method overestimates it by about 15%. With the finest grids the results are equal. A better overview can be seen if a single location is studied with varying grid spacing. Figure 12 presents the normalized friction coefficient drawn as a function of the height of the first row of cells (d_w^+). Skin-friction coefficients are taken at a local Reynolds number of $Re_x = 8 \times 10^5$. The present method clearly improves the results when $2 < d_w^+ < 13$. Accuracy is still very good at the value of the nondimensional height $d_w^+ = 7$.

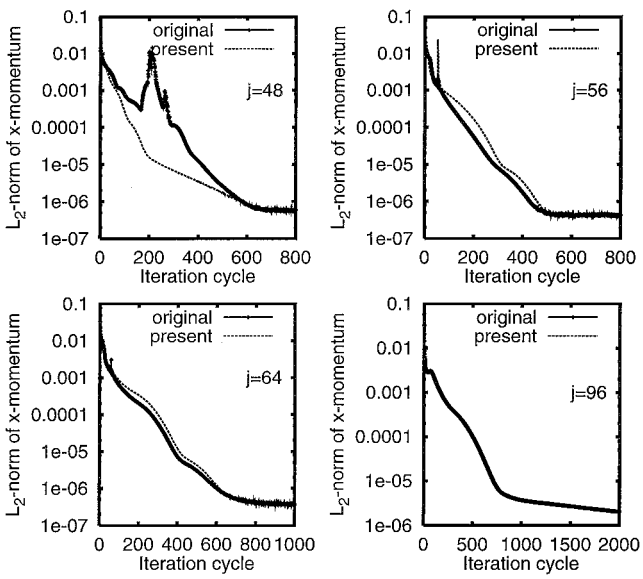

Fig. 10 Convergence with different grid sizes in the flat-plate simulation.

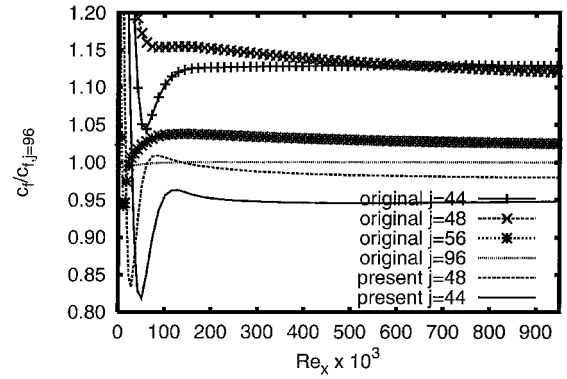

Fig. 11 Normalized friction coefficient (by the densest grid) as a function of Re_x: flat-plate simulation. Present model with 56 points is close to one and not shown here.

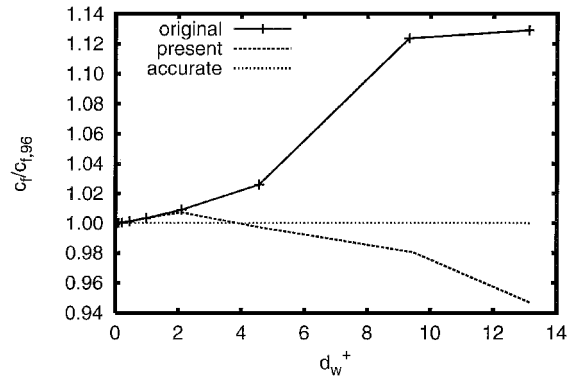

Fig. 12 Error in the friction coefficient as a function of d_w^+ at the location of $Re_x = 8 \times 10^5$.

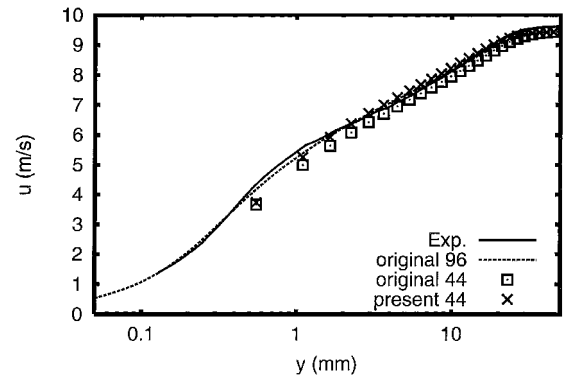

Fig. 13 Velocity profile at the location of $Re_x = 8 \times 10^5$.

The velocity profiles are shown with coarse grids in Fig. 13. Although the differences in friction coefficients are large, the differences in velocity profiles are smaller. Nevertheless, it can be seen that the new methods predict the velocity field better than the original one.

B. ONERA M6

As a three-dimensional case, a flow over the ONERA M6 wing[13] is simulated. The flow simulation is performed with $Ma = 0.84$, $\alpha = 3.06$ deg, and $Re = 11.72 \times 10^6$ based on mean aerodynamic chord ($c_{\text{mean}} = 2.7$ m). This case has been previously calculated by Siikonen et al.[14] with the present flow solver.

The simulation grid is an O-O-type grid with a size of $192 \times 80 \times 40$. The grid points used in the flow direction, from the wing surface, and in the spanwise direction are 192, 80, and 40, respectively. The height of the first row of the cells is less than 15 μm. The ratio of the heights between the neighboring cells

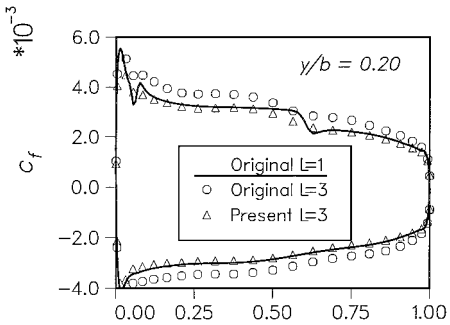

Fig. 14 Axial skin-friction coefficients for the ONERA M6 wing: —— is from the densest grid level, and the symbols from the coarsest (=third) level.

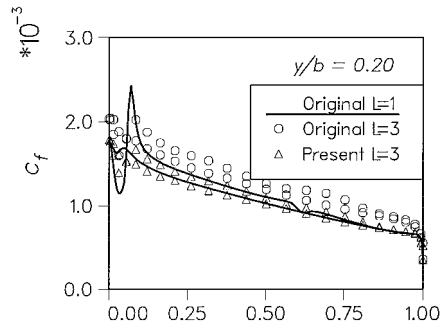

Fig. 15 Spanwise skin-friction coefficients for the ONERA M6 wing: —— is from the densest level, and the symbols from the coarsest level.

is $\Delta y_{j+1}/\Delta y_j = 1.19$. Simulations are also performed with two coarser grids. These grids are similar to the finest grid, but every other grid point in each direction is omitted. Grids in this calculation are called level 1 (with 614,400 points), level 2 (with 76,800 points), and level 3 (with 9600 points). The nondimensional height of the first row of the cells is of the order of $d_w^+ = 2$, 4, and 8 for different grids.

The skin-friction distribution with different grids for one wing section can be seen in Figs. 14 and 15. The calculated distributions are similar with the finest and even with the second finest grid level. Thus only one fine-grid result is plotted, and a comparison is made between the third-level results. The skin-friction coefficient is divided into axial and spanwise parts. In the preceding test cases the axial skin friction is shown to behave better with the present wall boundary conditions. It also seems to predict smaller skin frictions than the original one. A similar phenomenon is seen in Fig. 14. The spanwise skin-friction coefficient is shown in Fig. 15. The present method systematically predicts distributions closer to the finest grid result. It must be kept in mind that the biggest differences in the solutions with different grids are caused by different grid densities, not only in the direction perpendicular to the solid walls, but also in the axial and spanwise directions.

C. Hawk Trainer

As an engineering application, a flow past a jet trainer (BAe Hawk) is simulated using two different grid densities. In this case the coarser grid (level 3) is the same as the finer (level 2) except that every other grid point is omitted in each direction. The number of grid points is 51,232 or 409,856, respectively. The height of the first cell next to the surface is 2.4×10^{-5} m in the coarse grid and 10^{-5} m in the finer grid. These correspond to the average nondimensional heights of $y^+ = 6$ and $y^+ = 2.5$, respectively. The simulated flight condition is $Ma = 0.76$, $Re = 1.86 \times 10^7$ based on a wing aerodynamic mean chord, and $\alpha = 5.5$ deg.

The calculated lift and drag coefficients are presented in Table 1. The present model does not change the lift and drag coefficients considerably. Surprisingly, the lift coefficient is improved with the coarse grid. However, these modifications are expected to have a bigger effect on the drag. More detailed differences are seen by

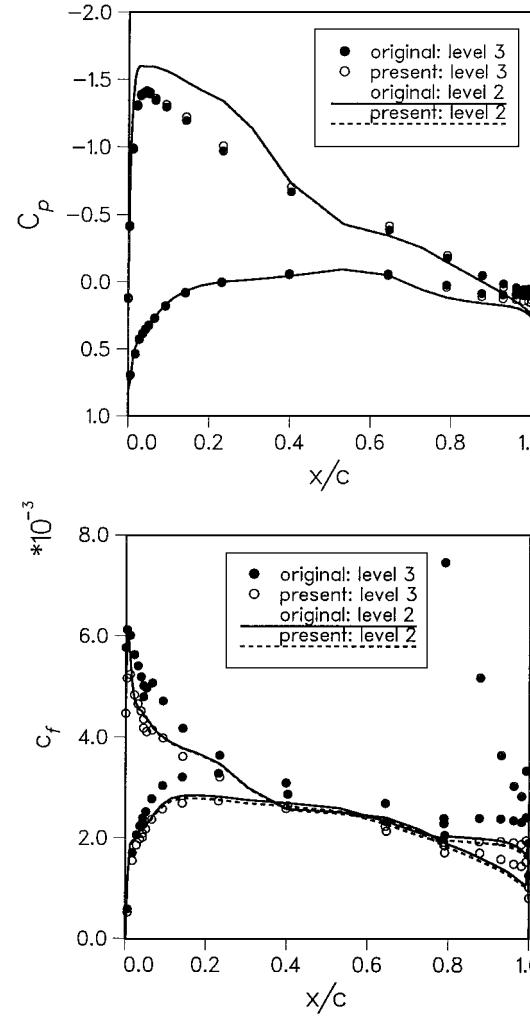

Fig. 16 Chordwise pressure and friction coefficient distributions obtained using different grid densities and different wall treatments at wing section $y/s \approx 0.25$.

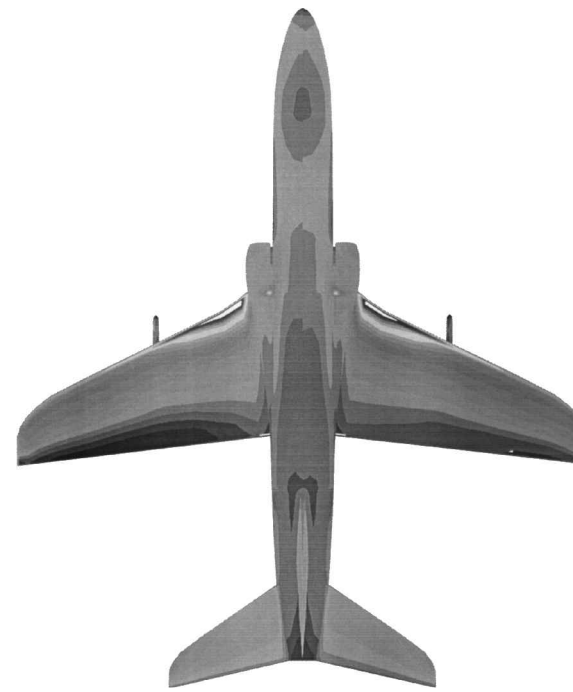

Fig. 17 Skin-friction fringes on the upper surface of the jet trainer. The left-hand side is simulated with the original method and the right-hand side with the present one. A coarse grid is used.

Table 1 Lift and drag coefficients for a jet trainer

	C_L		C_D	
Method	Coarse grid	Fine grid	Coarse grid	Fine grid
Original	0.599	0.699	0.0934	0.0738
Present	0.629	0.698	0.0935	0.0734

comparing the pressure and friction coefficients at one wing section in Fig. 16. The chordwise pressure coefficient distributions obtained using different grid densities and different wall treatments are presented at wing section $y/s \approx 0.25$, i.e., rather close to the wing root. The friction coefficient distributions are presented from the same location. Here the effect of the present model is clearly seen. Also the pressure coefficient is predicted better especially at the trailing-edge area. An overall comparison can be seen in Fig. 17, where the absolute value of the friction coefficient is drawn for the upper surface of the jet. The largest differences are at the trailing edge of the wing, but there are small differences everywhere.

V. Conclusions

The low-Reynolds-number models are sensitive to the height of the first row of the grid cells next to the solid walls. With careful modifications these restrictions can be reduced, but not removed. The proposed modifications can be made by presenting the gradients and source terms next to the solid walls more accurately, and also by taking into account the asymptotic behavior of different flow variables. The modifications made in this work have no effect on the results if the grid is dense enough. If the low-Reynolds-number model is used and the grid is coarse, the stability of the flow simulation can be poor. The stability limit can be raised if the boundary condition for the dissipation is well defined. The other modifications developed also increase the stability.

Present methods have been applied for a two-dimensional channel flow, a flat-plate boundary layer, the ONERA M6 wing, and a jet trainer. Results show superior accuracy especially for two-dimensional cases. In three-dimensional cases the solution is also improved, but not as much as in two-dimensional cases. This is probably because in the present three-dimensional tests the number of grid points is reduced also in other grid-line directions. In two-dimensional cases coarser grids are made by reducing only points perpendicular to the solid walls.

Compared to the original modeling, roughly three times larger cells next to the solid boundaries can be used in order to retain the same accuracy. Even with a very coarse grid the method gives satisfactory accuracy as far as skin friction is concerned. The new solid-wall boundary treatment is implemented with Chien's k–ϵ model. Because with coarse grids the biggest errors do not come from the turbulence model but from how the momentum equation and also the turbulent viscosity are treated, there is no restriction on the application of the present methods to other low-Reynolds-number two-equation models.

References

[1]Hanjalic, K., Hadzic, I., and Jakirlic, S., "Modelling Turbulent Wall Flows Subjected to Strong Pressure Variations," *Journal of Fluids Engineering*, Vol. 121, No. 1, 1999, pp. 57–64.

[2]Grotjans, H., and Menter, F., "Wall Functions for General Applications CFD Codes," *Proceedings of the Fourth ECCOMAS Conference*, edited by K. D. Papailiou, D. Tsahalis, J. Periaux, C. Hirsh, and M. Pandolfi, Wiley, New York, 1998, pp. 1112–1117.

[3]Chien, K.-Y., "Predictions of Channel and Boundary-Layer Flows with a Low-Reynolds-Number Turbulence Model," *AIAA Journal*, Vol. 20, No. 1, 1982, pp. 33–38.

[4]White, F. M., *Viscous Fluid Flow*, 2nd ed., McGraw–Hill, New York, 1991, p. 614.

[5]Kim, J., Moin, P., and Moser, R., "Turbulence Statistics in Fully Developed Channel Flow at Low Reynolds Number," *Journal of Fluid Mechanics*, Vol. 177, 1987, pp. 133–166.

[6]Hellsten, A., "Some Improvements in Menter's k–ω SST Turbulence Model," AIAA Paper 98-2554, June 1998.

[7]Durbin, P., "A Reynolds Stress Model for Near-Wall Turbulence," *Journal of Fluid Mechanics*, Vol. 249, 1993, pp. 465–498.

[8]Rautaheimo, P., and Siikonen, T., "Improved Solid-Wall Boundary Treatment in Low-Reynolds Number Turbulence Models," Lab. of Applied Thermodynamics, Rept. 122, Helsinki Univ. of Technology, Espoo, Finland, 1999.

[9]Siikonen, T., "An Application of Roe's Flux-Difference Splitting for the k–ϵ Turbulence Model," *International Journal for Numerical Methods in Fluids*, Vol. 21, No.11, 1995, pp. 1017–1039.

[10]Roe, P., "Approximate Riemann Solvers, Parameter Vectors, and Difference Schemes," *Journal of Computational Physics*, Vol. 43, No. 2, 1981, pp. 357–372.

[11]Van Albada, G., Van Leer, B., and Roberts, W., "A Comparative Study of Computational Methods in Cosmic Gas Dynamics," *Astronomy and Astrophysics*, Vol. 108, No. 76, 1982, pp. 76–84.

[12]Jameson, A., and Yoon, S., "Multigrid Solution of the Euler Equations Using Implicit Schemes," *AIAA Journal*, Vol. 24, No. 11, 1986, pp. 929–935.

[13]Schmitt, V., and Charpin, F., "Pressure Distributions on the ONERA M6-Wing at Transonic Mach Number," AR-138, AGARD, May 1979, pp. B1-1–B1-44.

[14]Siikonen, T., Kaurinkoski, P., and Laine, S., "Transonic Flow over a Delta Wing Using a k–ϵ Turbulence Model," *Proceedings of the 19th ICAS Congress*, 1994, pp. 700–710.

R. M. C. So
Associate Editor